Heterostructures Built in Metal Hydrides for Advanced Hydrogen Storage Reversibility

Yanran Wang, Xiaowei Chen, Hongyu Zhang, Guanglin Xia,* Dalin Sun, and Xuebin Yu*

Hydrogen storage is a vital technology for developing on-board hydrogen fuel cells. While $Mg(BH_4)_2$ is widely regarded as a promising hydrogen storage material owing to its extremely high gravimetric and volumetric capacity, its poor reversibility poses a major bottleneck inhibiting its practical applications. Herein, a facile strategy to effectively improve the reversible hydrogen storage performance of $Mg(BH_4)_2$ via building heterostructures uniformly inside MgH_2 nanoparticles is reported. The in situ reaction between MgH_2 nanoparticles and B_2H_6 not only forms homogeneous heterostructures with controllable particle size but also simultaneously decreases the particle size of the MgH_2 nanoparticles inside, which effectively reduces the kinetic barrier that inhibits the reversible hydrogen storage in both $Mg(BH_4)_2$ and MgH_2. More importantly, density functional theory coupled with ab initio molecular dynamics calculations clearly demonstrates that MgH_2 in this heterostructure can act as a hydrogen pump, which drastically changes the enthalpy for the initial formation of B—H bonds by breaking stable B—B bonds from endothermic to exothermic and hence thermodynamically improves the reversibility of $Mg(BH_4)_2$. It is believed that building heterostructures provides a window of opportunity for discovering high-performance hydrogen storage materials for on-board applications.

Hydrogen has been considered as a sustainable and clean energy carrier that promises environmentally friendly energy sources capable of supplying the ever-increasing global energy demands.[1] Unfortunately, the efficient and safe storage of hydrogen with high gravimetric and volumetric capacity poses a major economical bottleneck for the adoption of hydrogen.[2–7] Magnesium borohydride ($Mg(BH_4)_2$), which exhibits an extremely high gravimetric capacity of 14.9 wt% and volumetric capacity of 145–147 kg cm^{-3}, has been widely regarded as a promising hydrogen storage material.[8–11] More importantly, an enthalpy change of -39 kJ mol^{-1} H_2 was theoretically calculated

for the dehydrogenation of $Mg(BH_4)_2$ to form MgB_2, which is equivalent to the release of 1 atm H_2 at temperatures of 20–75 °C, which is suitable for practical application in proton-exchange membrane fuel cells.[12–14] The high kinetic energy barriers resulting from the sluggish diffusion of hydrogen and mass transport, however, cause the operating storage temperature to rise over 300 °C.[15–18] Moreover, the reversibility of $Mg(BH_4)_2$ that could be achieved was only partial, even under an extreme condition of 950 bar H_2 at 400 °C, which is impractical for many applications, and this poses a major barrier for the future application of $Mg(BH_4)_2$ as hydrogen storage materials.[19,20]

Space-confining $Mg(BH_4)_2$ into porous substrates has been demonstrated as a direct and effective method for improving the hydrogen storage performance of $Mg(BH_4)_2$. This method can significantly reduce their particle size, and hence reduce the barrier that inhibits hydrogen and mass transport during the solid-state transformation process.[21–24] In addition, the introduction of support materials could inhibit the particle growth and agglomeration of $Mg(BH_4)_2$, enhancing the cycling stability.[25] Moreover, the space-confinement of $Mg(BH_4)_2$ could promote the formation of MgB_2, which is thermodynamically capable of being hydrogenated directly to form $Mg(BH_4)_2$; hence, the reversibility of $Mg(BH_4)_2$ can be improved to some extent.[26] However, owing to the high energy required to break stable B—B bonds and the large diffusion barrier of H in MgB_2, the reversible ratio is still lower than 20% even under a pressure as high as 15 MPa.[27] Another method for improving the reversibility of $Mg(BH_4)_2$ is to mechanically mill MgB_2 with Mg/MgH_2 in solvents.[28] Although milling process creates defects that improve the reversibility of MgB_2 to some extent, the physical contact between Mg/MgH_2 and MgB_2 was largely limited owing to the uncontrollable distribution with large particle size; more importantly, only the first cycle of hydrogen storage could be achieved owing to the difficult formation of MgB_2 via the direct dehydrogenation of bulk $Mg(BH_4)_2$. In addition, the adsorption of solvents degrades the performance of the as-synthesized composites, possibly pollutes the released hydrogen, and reduces the suitability of the hydrogenation process for on-board hydrogen storages.

In this work, in order to simultaneously facilitate the formation and the hydrogen storage reversibility of MgB_2, a unique

Y. Wang, H. Zhang, Dr. G. Xia, Prof. D. Sun, Prof. X. Yu
Department of Materials Science
Fudan University
Shanghai 200433, China
E-mail: xiaguanglin@fudan.edu.cn; yuxuebin@fudan.edu.cn
Prof. X. Chen
Department of Physics
Jimei University
Xiamen 361021, China

**ADVANCED
SCIENCE NEWS**
www.advancedsciencenews.com

**ADVANCED
MATERIALS**
www.advmat.de

heterostructure of $Mg(BH_4)_2@MgH_2$ was constructed, wherein $Mg(BH_4)_2$ nanoparticles (NPs) were in situ built on MgH_2 NPs uniformly via the solid–gas reaction between MgH_2 and B_2H_6 (**Figure 1**a). The building of heterostructures with an average particle size of approximately 10 nm could not only realize the formation of $Mg(BH_4)_2$ NPs, but also serve as an effective way to chemically tune the particle sizes of both MgH_2 and the as-formed $Mg(BH_4)_2$ NPs, which further reduces their respective hydrogen storage temperature and increases systematic reversible hydrogen storage density. In addition, the controllable tuning of particle size of $Mg(BH_4)_2$ within <1 nm leads to the efficient formation of MgB_2 upon the dehydrogenation of $Mg(BH_4)_2$ at a moderate temperature, which provides a plausible thermodynamic solution for improving the reversibility of the hydrogen storage of $Mg(BH_4)_2$. More interestingly, it was theoretically and experimentally validated that the presence of MgH_2 may act as a hydrogen pump, which could affect the enthalpy for the initial formation of B−H bonds such

that breaking the stable B−B bonds becomes an exothermic process; this thermodynamically improves the reversibility of $Mg(BH_4)_2$ significantly. As a result, the synergistic improvement in thermodynamics and kinetics facilitates the building of heterostructures that increase the reversible ratio of $Mg(BH_4)_2$ to approximately 70%. Coupled with the stable reversibility of MgH_2 NPs, the as-built $Mg(BH_4)_2@MgH_2$ nanoparticles could exhibit a stable systematic hydrogen capacity of approximately 4.8 wt% after eight cycles.

As shown in Figure 1, graphene-supported homogeneous MgH_2 nanoparticles (MgH_2/G) with an average particle size of 8.5 nm were synthesized via hydrogenation-induced self-assembly (Figure S1, Supporting Information). High-resolution transmission electron microscopy (HRTEM) images revealed a typical d-spacing of 0.25 nm, which could be indexed to the (101) planes of hexagonal MgH_2, indicating the formation of MgH_2 NPs. This is in good agreement with X-ray diffraction (XRD) patterns (Figure S2, Supporting Information). The uniform
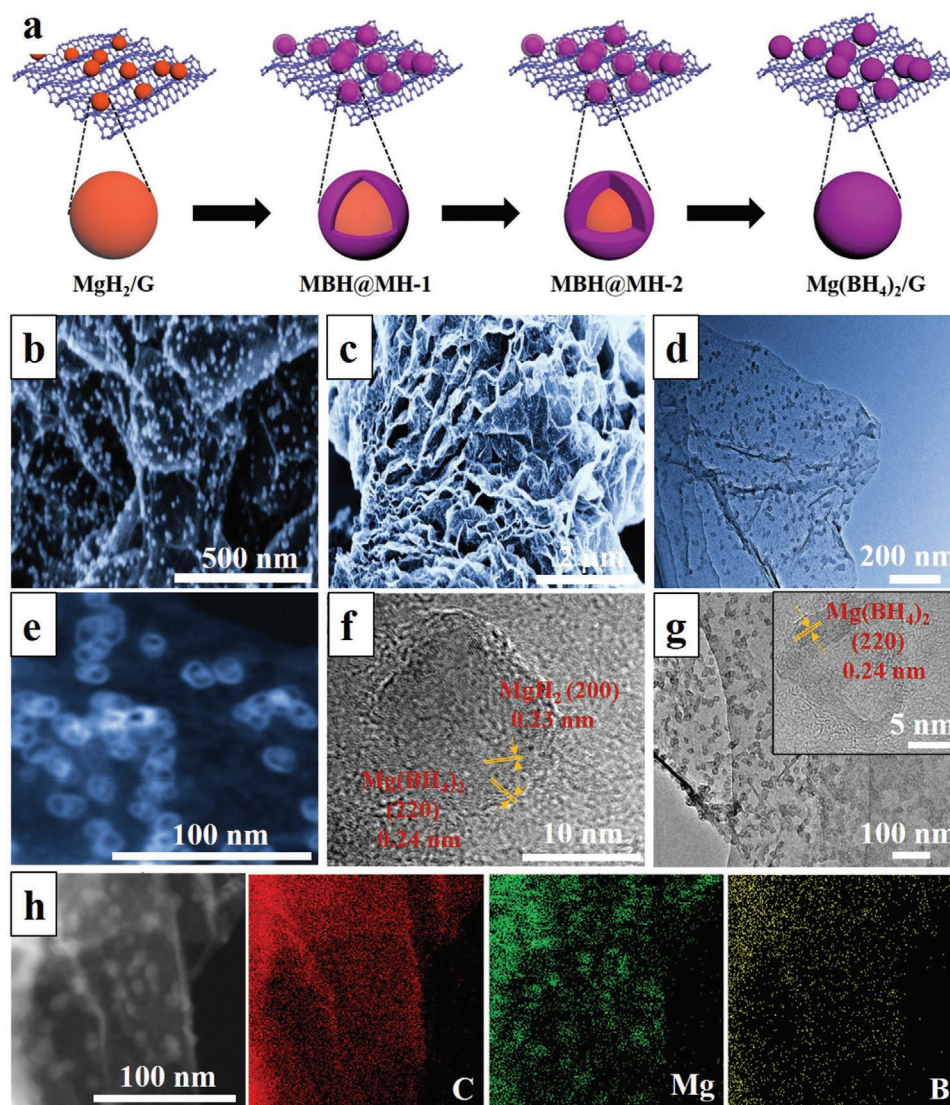

Figure 1. a) Schematic illustration of the synthesis of $Mg(BH_4)_2@MgH_2$ NPs on graphene. b,c) SEM, d) TEM, e) STEM, and f) HRTEM images of MBH@MH-2. g) TEM image of $Mg(BH_4)_2$/G. h) Elemental mapping of MBH@MH-2.

**ADVANCED
SCIENCE NEWS**

www.advancedsciencenews.com

**ADVANCED
MATERIALS**

www.advmat.de

distribution of MgH_2 NPs on flexible graphene layers could not only ensure the high loading of MgH_2 NPs and facilitate the subsequent chemical reaction between MgH_2 and B_2H_6, leading to a high systematic hydrogen storage density, but also contribute to preserving the structural integrity. Upon proceeding for 2 h, the reaction between MgH_2 and B_2H_6 (denoted as MBH@MH-1) resulted in the weakening of the intensity of characteristic XRD peaks belonging to MgH_2, and X-ray photoelectron spectroscopy (XPS) spectra clearly demonstrated the high purity of the as-synthesized MBH@MH-1 with the appearance of B-containing species (Figure S3a, Supporting Information). Although there were no visible peaks belonging to $Mg(BH_4)_2$ in the XRD results, the formation of $Mg(BH_4)_2$ could be evidenced by the presence of characteristic peaks of $Mg(BH_4)_2$ in the high-resolution XPS B 1s spectra (Figure S3b, Supporting Information) and by the characteristic B−H bonds in the Fourier transform infrared spectroscopy (FTIR) spectra (Figure S4, Supporting Information). The coexistence of MgH_2 and $Mg(BH_4)_2$ in the XRD patterns (Figure S2, Supporting Information) as well as FTIR spectra (Figure S4, Supporting Information) could be verified in the composite after prolonging the reaction time to 5 h (denoted as MBH@MH-2). Moreover, it could be clearly observed that, with graphene providing the structural support, the distribution of MgH_2 NPs was homogeneous (Figures 1a–c) with the formation of partial hollow structures inside (Figure 1d). These hollow structures could be attributed to the Kirkendall effect resulting from the different diffusion speeds of Mg and BH-containing species. HRTEM image verifies the presence of characteristic d-spacings of MgH_2 and $Mg(BH_4)_2$ (Figure 1e), illustrating the formation of $Mg(BH_4)_2$ on the surface of MgH_2 NPs (denoted as MBH@MH), which simultaneously reduces the particle size of MgH_2 NPs inside to some extent. In addition, it should be noted that due to the introduction of B_2H_6, the average particle size of nanoparticles was slightly increased to approximately 10.0 nm (Figure S5, Supporting Information). To characterize the particle size of thus-formed $Mg(BH_4)_2$ NPs, the as-synthesized $Mg(BH_4)_2$@MgH_2 composite was washed by tetrahydrofuran, which is a good solvent for $Mg(BH_4)_2$. After the washing process, FTIR spectra clearly illustrated the absence of characteristic peaks of B−H bonds indexed to $Mg(BH_4)_2$ (Figure S6, Supporting Information), which provides additional evidence proving the formation of $Mg(BH_4)_2$ with high purity after the reaction between MgH_2 and B_2H_6. The decrease in particle sizes of MBH@MH NPs induced by the removal of $Mg(BH_4)_2$ were analyzed: the average particle size of $Mg(BH_4)_2$ in MBH@MH-1 and MBH@MH-2 could be indirectly verified to be lower than 0.7 and 1.1 nm, respectively (Figures S5 and S7, Supporting Information). This demonstrates that building heterostructures of $Mg(BH_4)_2$ on MgH_2 NP is an effective way not only to fabricate $Mg(BH_4)_2$ NPs but also to tune the particle size of both $Mg(BH_4)_2$ and MgH_2 in a facile manner. The corresponding elemental mapping validates the uniform distribution of Mg, B, and C in the as-synthesized MBH@MH-2, providing further evidence to the homogeneous distribution of $Mg(BH_4)_2$@MgH_2 NPs on the graphene layers. Upon prolonging the reaction time to 12 h, MgH_2 NPs were transformed into $Mg(BH_4)_2$ completely (denoted as MBH/G), as evidenced by the XRD and FTIR results (Figures S2 and S4, Supporting Information).

The hydrogen storage performance of MBH@MH composites was first evaluated by thermogravimetric analysis (TGA) coupled with mass spectra (MS). The peak temperature for the hydrogen desorption from bulk $Mg(BH_4)_2$ reaches 329 °C, accompanied by a minor peak at 432 °C (Figure S8, Supporting Information), indicating the multistep decomposition of $Mg(BH_4)_2$ before 500 °C. By comparison, the addition of graphene could reduce the peak dehydrogenation temperature down to 316 °C with the completion of the main dehydrogenation process before 400 °C, which validates the catalytic role of graphene in improving the hydrogen desorption performance of $Mg(BH_4)_2$. However, the addition of MgH_2 into the composite of $Mg(BH_4)_2$ and graphene (denoted as MBH-MH-G) resulted in the peak temperature for the dehydrogenation of MgH_2 and $Mg(BH_4)_2$ as well as that for the dehydrogenated product after heating to 500 °C to be comparable to that of the bulk MgH_2-G and $Mg(BH_4)_2$-G, indicating that there was no chemical interaction between MgH_2 and $Mg(BH_4)_2$ during the dehydrogenation process (Figure S9, Supporting Information). Showing strong contrast, MgH_2/G could release 4.3 wt% hydrogen with a peak temperature at approximately 253 °C, whereas the hydrogen released from $Mg(BH_4)_2$/G, owing to the introduction of B_2H_6, could reach 8.9 wt% with a lower peak temperature of 200 °C (**Figure 2**a,b) due to the significant decrease in particle size down to nanometer scale. More interestingly, utilizing heterostructures facilitated the extra reduction of particle size of both $Mg(BH_4)_2$ and MgH_2 NPs relative to pure $Mg(BH_4)_2$/G or MgH_2/G, simultaneously lowering their characteristic peak temperature down to 191 and 242 °C for MBH@MH-1 and 197 and 234 °C for MBH@MH-2, respectively. This result directly verifies that the facile-tuned particle size via building heterostructures of $Mg(BH_4)_2$ on MgH_2 NP synergistically decreases the dehydrogenation temperature due to the reduction of particle size of both $Mg(BH_4)_2$ and MgH_2. Consequently, the significant decrease in the dehydrogenation temperature of both MgH_2 and $Mg(BH_4)_2$ in the MBH@MH composite could be mainly attributed to the significant reduction of particle size to the nanometer scale and their uniform distribution on graphene, which exhibits a catalytic effect. Based on their separate dehydrogenation temperature, the amount of hydrogen desorbed from $Mg(BH_4)_2$ and MgH_2 in MBH@MH-1 was approximately 2.8 and 3.4 wt%, respectively, and 5.1 and 2.5 wt% for MBH@MH-2.

XRD results demonstrate that the dehydrogenation products of the MBH@MH composite at 300 °C were mainly composed of MgB_2 and Mg (Figure S10, Supporting Information), accompanied with the complete disappearance of B−H peaks in FTIR spectra (Figure S11, Supporting Information). It not only verifies the complete hydrogen desorption but also further proves the noninteraction among the dehydrogenation process between MgH_2 and $Mg(BH_4)_2$ upon heating on the nanometer scale. By comparison, only minor MgB_2 was observed in the bulk composite of $Mg(BH_4)_2$ and graphene with or without the presence of MgH_2 (Figure S9, Supporting Information), accompanied with residual $MgB_{12}H_{12}$ after heating to an even higher temperature of 500 °C (Figure S12, Supporting Information). The formation of $MgB_{12}H_{12}$, Mg, and amorphous boron with high thermodynamic stability after dehydrogenation would significantly decrease the reversibility of hydrogenation of the
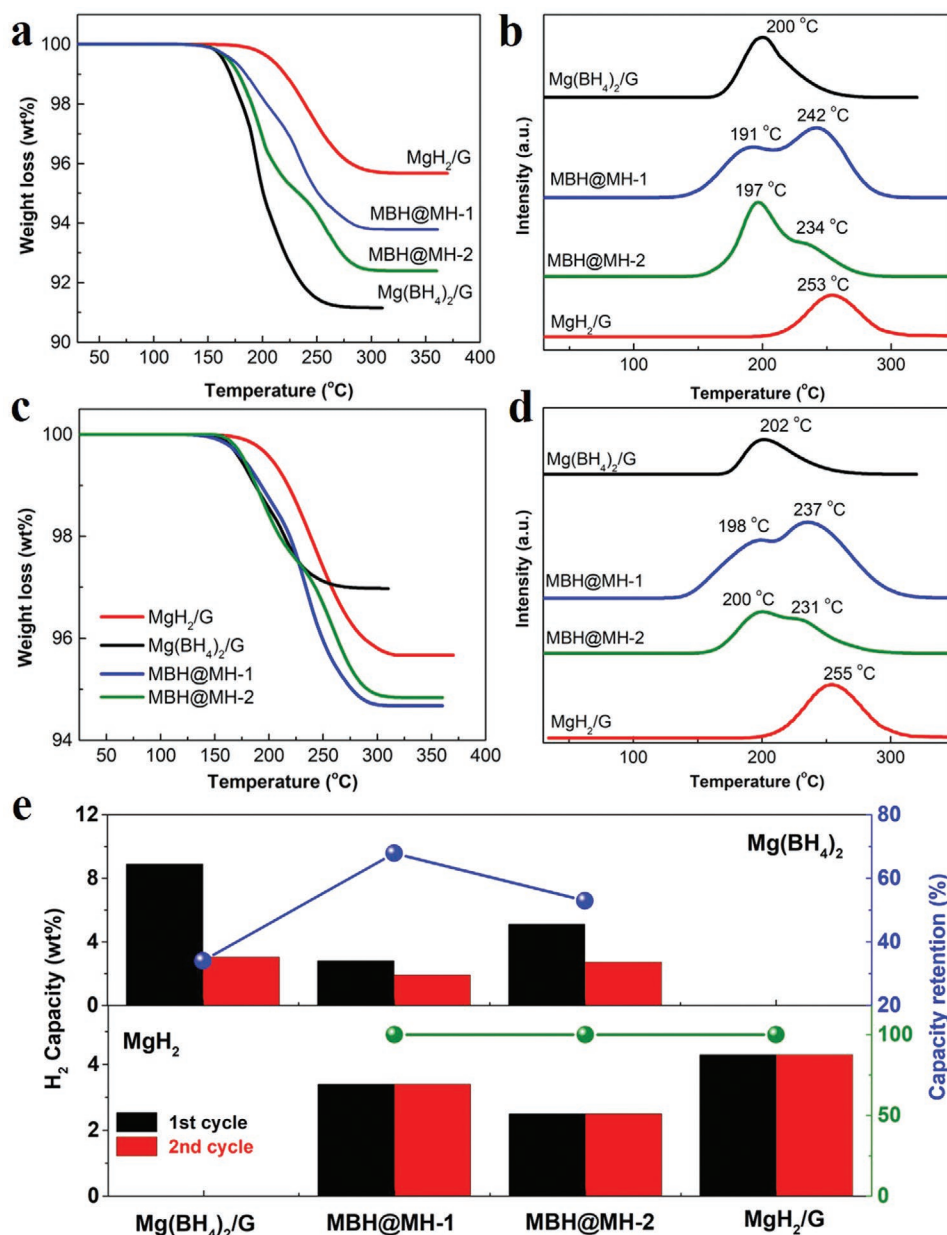
ADVANCED
SCIENCE NEWS
www.advancedsciencenews.com

ADVANCED
MATERIALS
www.advmat.de

Figure 2. a) TGA and b) MS results of the as-synthesized MBH@MH-1 and MBH@MH-2, including MgH_2/G and $Mg(BH_4)_2$/G for comparison. c) TGA and d) MS results of MBH@MH-1 and MBH@MH-2 after the first cycle of hydrogenation process, including MgH_2/G and $Mg(BH_4)_2$/G for comparison. e) Normalized reversible ratio of MgH_2 and $Mg(BH_4)_2$ in MBH@MH-1 and MBH@MH-2, including MgH_2/G and $Mg(BH_4)_2$/G for comparison, where the hydrogen capacities are normalized to the dehydrogenation capacity exhibited in the first cycle.

whole system.[29] As a result, only negligible reversibility could be achieved for bulk $Mg(BH_4)_2$-G and MBH-MH-G after the initial reversible charge of hydrogen (Figure S13, Supporting Information). By comparison, a capacity of approximately 3 wt% was obtained for the $Mg(BH_4)_2$/G, corresponding to a capacity retention of only 34%, with the observation of abundant MgB_2 in the dehydrogenated products of $Mg(BH_4)_2$/G, which could be attributed to the sluggish mass transportation and stable B—B bonds of MgB_2.[30] More interestingly, it could be clearly observed that upon partial transformation, the reversible hydrogen capacity of MBH@MH composites could

be further enhanced to a value that is much higher than that of both MgH_2/G and $Mg(BH_4)_2$/G. Particularly, the reversible capacity of MBH@MH-1 reached as high as 5.3 wt%, with 1.9 wt% for $Mg(BH_4)_2$ and 3.4 wt% for MgH_2. The complete reversibility of MgH_2 was maintained in the composite, and the capacity retention of $Mg(BH_4)_2$ in MBH@MH-1 and MBH@MH-2 was upgraded to 68% and 53%, respectively, much higher than that of $Mg(BH_4)_2$/G. After the hydrogenation process, the formation of $Mg(BH_4)_2$ and MgH_2 could be directly verified for MBH@MH composite, accompanied with the complete disappearance of MgB_2 in the XRD results (Figures S14 and S15,

**ADVANCED
SCIENCE NEWS**

www.advancedsciencenews.com

**ADVANCED
MATERIALS**

www.advmat.de

Supporting Information). By comparison, although FTIR spectra validated the partial formation of $Mg(BH_4)_2$, there were evident characteristic peaks belonging to MgB_2 in the rehydrogenated $Mg(BH_4)_2/G$, indicating the limited reversibility of pure $Mg(BH_4)_2$ NPs, which corresponds with its low reversible ratio of approximately 34% (Figure S14, Supporting Information). It provides direct evidence to the significantly enhanced reversibility by building heterostructures of $Mg(BH_4)_2@MgH_2$ NPs, which could simultaneously tune the particle size of $Mg(BH_4)_2$ and MgH_2 NPs.

In addition to that of the structural effect, we investigated the direct effect of MgH_2 on improving the reversibility of MgB_2, which is the dehydrogenated product of $Mg(BH_4)_2$ NPs, by mixing MgH_2 with MgB_2 particles. Surprisingly, with the addition of MgH_2, the reversible capacity of MgB_2 could be increased remarkably to 12.3% from the 3.4% of pure MgB_2 (Figure S16, Supporting Information), accompanied by the weak but detectable formation of B−H bonds (Figure S17, Supporting Information), which demonstrates that the presence of MgH_2 also plays an important role in improving the reversible hydrogen storage of MgB_2. In order to unravel the mechanism behind this, first-principle calculations were conducted based on density functional theory. The calculations reveal that under a stable structural configuration, the clear formation of numerous B−H bonds can be observed on MgB_2 under the support of MgH_2, formed due to the transfer of hydrogen from MgH_2 to form Mg atoms, (Figure 3a,b). This demonstrates that MgH_2 could act as hydrogen pump to facilitate the initial hydrogenation of MgB_2. In order to better understand the mechanism of this hydrogenation process, ab initio molecular dynamics (AIMD) simulations were further conducted (**Figure 3**c). Initially, one layer of MgB_2 was deposited on the top surface of MgH_2 matrix after structural modification; as the simulation proceeded, all hydrogen atoms moved toward a low-energy configuration (Movie S1, Supporting Information). It directly demonstrates the transfer of hydrogen from MgH_2 matrix after only 3 ps from the start of the simulation, leading to the further breaking of B−B bonds in MgB_2 and the favorable formation of B−H bonds. The number of B−H bonds significantly increased as the simulation time increased from 3 to 15 ps, indicating the favorable formation of B–H bonds induced by the transfer of hydrogen from MgH_2 as the structural support. More interestingly, under the structural support of MgH_2, the subsequent absorption of hydrogen on MgB_2 was energetically favorable, with an enthalpy of −2.99 eV (Figure 3d). Contrastingly, despite the thermodynamically favorable hydrogen storage reaction of MgB_2 to form $Mg(BH_4)_2$, the initial adsorption of H on MgB_2 via the breakage of stable B−B bonds was instead an endothermic process with an enthalpy of 0.117 eV (Figure 3e). This indicates that the building of heterostructures could thermodynamically promote the hydrogenation of MgB_2 through the formation of B−H bonds owing to the transfer of hydrogen from MgH_2, which significantly enhanced the reversibility of MgB_2. Coincidentally, the building of heterostructures via the in situ formation of $Mg(BH_4)_2$ on MgH_2 NPs could ensure the homogeneous and intimate contact between MgH_2 and $Mg(BH_4)_2$, which could largely affect the potential and hence lead to significantly improved reversibility of $Mg(BH_4)_2$.
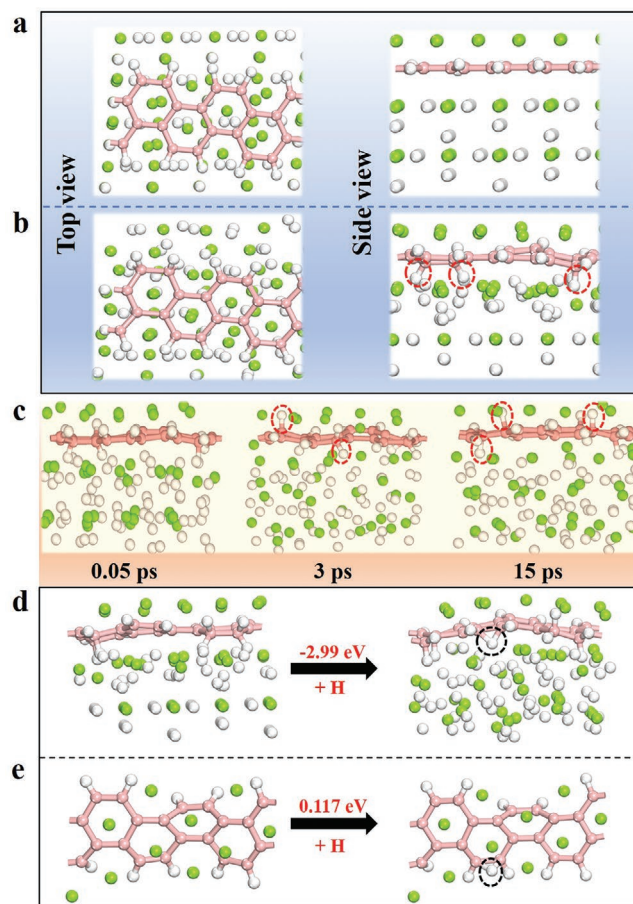

Figure 3. Top view and side view of the adsorption configuration of MgB_2 under the support of MgH_2 before (a) and after (b) structural modification, in which the thus-formed B−H bonds are highlighted by red circles. c) Snapshot of the AIMD simulation of the hydrogenation process of MgB_2 under the support of MgH_2, in which the thus-formed B−H bonds via the transfer of hydrogen from MgH_2 are highlighted by red circles. Calculated hydrogen absorption energy on MgB_2 with (d) and without (e) the presence of MgH_2 as the structural support. The Mg, B, and H atoms are shown in green, pink, and white spheres, respectively.

In an ideal hydrogen storage system, the reversibility of hydrogenation and dehydrogenation must be efficient even under moderate conditions. Hence, the long-term cycling hydrogen storage performance of $Mg(BH_4)_2$ was subsequently measured through isothermal hydrogenation and dehydrogenation at 260 °C via the volumetric method. As shown in **Figure 4**a, the presence of graphene as the structural support could realize the stable reversibility of MgH_2/G, exhibiting a capacity retention of approximately 99.8% after five cycles. In the terms of MBH@MH-2, after partial transformation of MgH_2 into $Mg(BH_4)_2$, although the initial storage capacity is much higher than MgH_2/G, a reversible capacity ratio of only 58.6% could be preserved after five cycles of hydrogenation and dehydrogenation processes, owing to the limited reversibility of $Mg(BH_4)_2$. In strong contrast, the enhanced reversibility of $Mg(BH_4)_2$ via tuning the heterostructures of $Mg(BH_4)_2@MgH_2$ caused the reversible capacity of MBH@MH-1 after five cycles to reach 4.92 wt%, which was 12% higher than that of MgH_2/G.

**ADVANCED
SCIENCE NEWS**

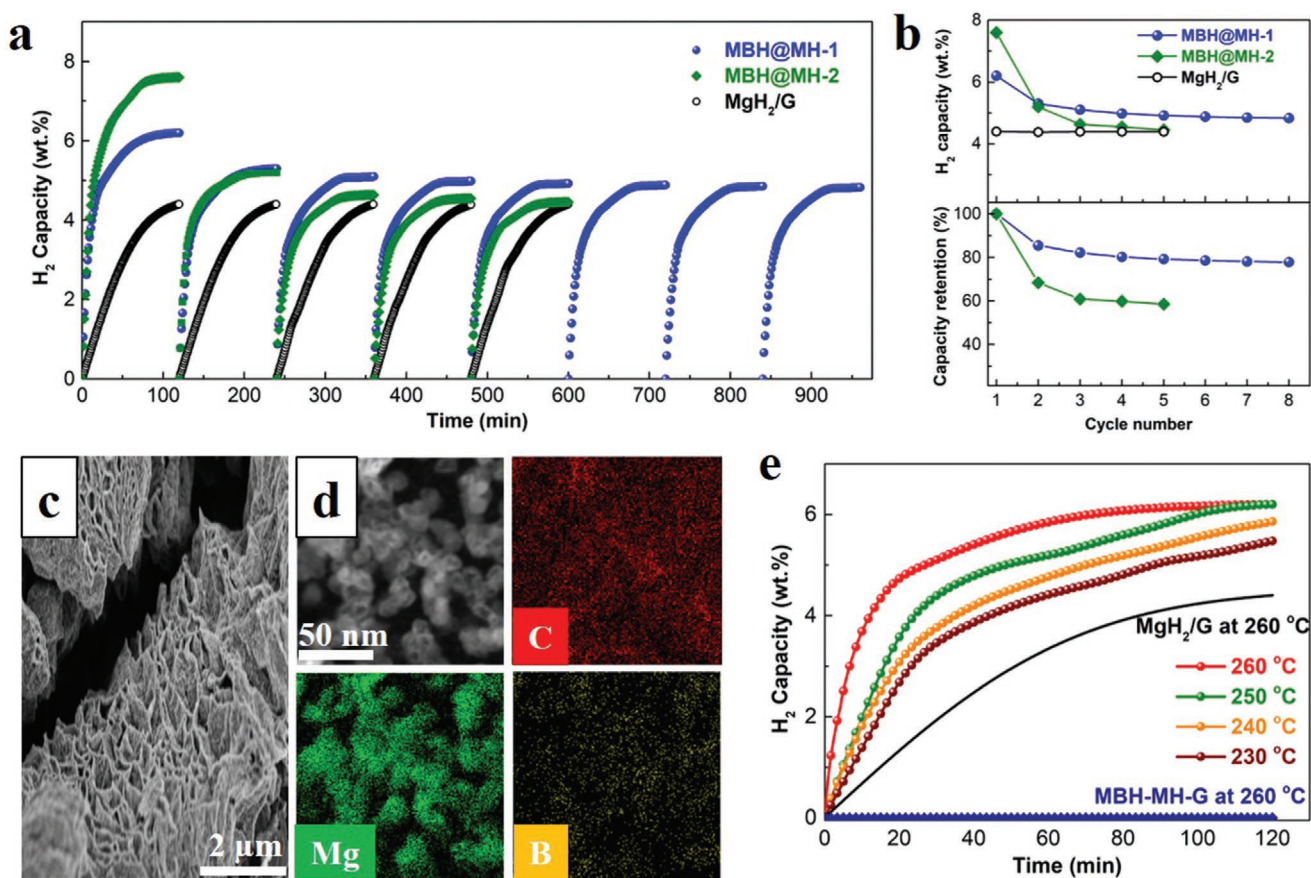www.advancedsciencenews.com

**ADVANCED
MATERIALS**

www.advmat.de

Figure 4. a) Cycling performance and b) normalized hydrogen desorption capacity of MBH@MH composites, with MgH$_2$/G included for comparison. c) SEM and d) STEM image with the corresponding elemental mapping of MBH@MH-1 after eight cycles of hydrogen storage process. e) Isothermal dehydrogenation kinetics of MBH@MH-1 at various temperatures, with MgH$_2$/G and the ball-milled composite of MBH-MH-G at 260 °C included for comparison.

This value could be maintained at 4.83 wt% after eight cycles, corresponding to a capacity retention of 91.1% after the second cycle. SEM and TEM images validate that graphene, as the structural support helped preserve the homogeneous distribution of MBH@MH composite on graphene in MBH@MH-1 after the cycling performance. No evident agglomeration and particle growth could be observed for the MBH@MH NPs with an average particle size of 9.7 nm (Figure S18, Supporting Information). These structural features could effectively facilitate the transfer of hydrogen and shorten the diffusion pathway of hydrogen and mass transport, which contributes to enhancing the reversibility of both Mg(BH$_4$)$_2$ and MgH$_2$.

Isothermal volumetric dehydrogenation values were measured at various temperatures to evaluate the hydrogen desorption kinetics of MBH@MH composites (Figure 4e). At a temperature of 260 °C, no hydrogen release could be observed for the bulk composite of MgH$_2$, Mg(BH$_4$)$_2$, and graphene, and 4.4 wt% of hydrogen could be released from MgH$_2$/G owing to the significant reduction of particle size down to the nanometer scale. By comparison, a complete dehydrogenation process could be achieved for MBH@MH-1 under less than 80 min, equaling to a hydrogen desorption capacity of 6.2 wt%, indicating the full dehydrogenation of both MgH$_2$ and Mg(BH$_4$)$_2$ with help from the reduction in particle size. Moreover, upon decreasing the

temperature down to only 230 °C, MBH@MH-1 was capable of releasing approximately 5.5 wt% hydrogen within 120 min, which is much higher than that of MgH$_2$/G even at 260 °C. In order to quantitatively characterize the improved dehydriding kinetics, the apparent activation energies (E_a) of MBH@MH-1 were subsequently calculated based on the Arrhenius equation (Figure S19, Supporting Information). After fitting the experimental data at various temperatures, the E_a for the dehydrogenation of MBH@MH-1 was calculated to be 90.6 kJ mol^{-1}, which is much lower than the same value for both their bulk counterparts and pure nanosized MgH$_2$ with the support of a carbon matrix (118.9 kJ mol^{-1} for MgH$_2$ NPs on graphene).[31] By accounting for the cycling stability, the reversible capacity, as well as the operating temperature, the MBH@MH NPs in this study is among the best reported Mg(BH$_4$)$_2$-based hydrogen storage materials so far (Table S1, Supporting Information). The superior hydrogen storage performance of MBH@MH-1 could be mainly attributed to several unique features. First, the Mg(BH$_4$)$_2$ heterostructures layers built on MgH$_2$ NPs with an overall particle size of ≈10 nm could effectively control the particle sizes of both MgH$_2$ and Mg(BH$_4$)$_2$, thereby lowering their respective hydrogenation/dehydrogenation temperature and maintaining high hydrogen storage capacity. Upon dehydrogenation, the thus-formed Mg(BH$_4$)$_2$ NPs with a particle size less

than ≈1 nm promoted the efficient formation of MgB_2 at a moderate temperature, which offers a thermodynamic prerequisite for the reversible formation of $Mg(BH_4)_2$. More importantly, the close and homogeneous contact between MgB_2 and MgH_2 could further promote the reversibility of $Mg(BH_4)_2$, thermodynamically enhancing the reversible formation of B−H bonds by breaking stable B−B bonds of MgB_2. Additionally, the uniform distribution of graphene provided stable structural support for alleviating the growth and agglomeration of MBH@MH NPs, which contributed to the enhancement of cycling stability. As a consequence, the designed MBH@MH NPs exhibited advanced hydrogen storage performance with respect to the kinetics, thermodynamics, and stable cycling performance with high hydrogen storage capacity.

In summary, we have discovered a facile strategy for improving the reversible hydrogen storage performance of Mg-based hydrides by building heterostructures of $Mg(BH_4)_2$ on MgH_2, which was demonstrated to be an effective way to simultaneously control the particle sizes of both MgH_2 and $Mg(BH_4)_2$ NPs, leading to the improved kinetics for hydrogen storage. In addition, the controllable tuning of particle size of $Mg(BH_4)_2$ within the region less than ≈1 nm leads to the efficient formation of MgB_2 upon the dehydrogenation of $Mg(BH_4)_2$ at moderate temperature. Moreover, the presence of MgH_2 acted as a hydrogen pump, effectively reducing the energy required for the initial formation of B−H bonds and hence thermodynamically improving the reversibility of $Mg(BH_4)_2$. Owing to the synergistic effect on tuning thermodynamics and kinetics, the as-built $Mg(BH_4)_2@MgH_2$ nanoparticles exhibited a stable systematic hydrogen capacity of approximately 4.8 wt% at a low temperature of 260 °C after eight cycles. Our study on the heterostructures reported herein may also enlighten the interests on the interface chemistry research to improve the hydrogen storage performance of metal hydrides for practical applications.

Supporting Information

Supporting Information is available from the Wiley Online Library or from the author.

Conflict of Interest

The authors declare no conflict of interest.

[1] L. Schlapbach, *Nature* **2009**, *460*, 809.
[2] R. Mohtadi, S.-i. Orimo, *Nat. Rev. Mater.* **2017**, *2*, 16091.
[3] M. B. Ley, L. H. Jepsen, Y.-S. Lee, Y. W. Cho, J. M. Bellosta von Colbe, M. Dornheim, M. Rokni, J. O. Jensen, J. Sloth, Y. Filinchuk, J. E. Jørgensen, F. Besenbacher, T. R. Jensen, *Mater. Today* **2014**, *17*, 122.
[4] L. Z. Ouyang, W. Chen, J. W. Liu, M. Felderhoff, H. Wang, M. Zhu, *Adv. Energy Mater.* **2017**, *7*, 1700299.
[5] A. Schneemann, J. L. White, S. Kang, S. Jeong, L. F. Wan, E. S. Cho, T. W. Heo, D. Prendergast, J. J. Urban, B. C. Wood, M. D. Allendorf, V. Stavila, *Chem. Rev.* **2018**, *118*, 10775.
[6] Y. Jia, C. Sun, S. Shen, J. Zou, S. S. Mao, X. Yao, *Renewable Sustainable Energy Rev.* **2015**, *44*, 289.
[7] Y. Y. Zhu, L. Z. Ouyang, H. Zhong, J. W. Liu, H. Wang, H. Y. Shao, Z. G. Huang, M. Zhu, *Angew. Chem., Int. Ed.* **2020**, *59*, 8623.
[8] M. Paskevicius, L. H. Jepsen, P. Schouwink, R. Cerny, D. B. Ravnsbaek, Y. Filinchuk, M. Dornheim, F. Besenbacher, T. R. Jensen, *Chem. Soc. Rev.* **2017**, *46*, 1565.
[9] Z. Huang, T. Autrey, *Energy Environ. Sci.* **2012**, *5*, 9257.
[10] Y. Liu, Y. Yang, Y. Zhou, Y. Zhang, M. Gao, H. Pan, *Int. J. Hydrogen Energy* **2012**, *37*, 17137.
[11] Y. Luo, Q. Wang, J. Li, F. Xu, L. Sun, Y. Zou, H. Chu, B. Li, K. Zhang, *Mater. Today Nano* **2020**, *9*, 100071.
[12] Y. Liu, Y. Yang, M. Gao, H. Pan, *Chem. Rec.* **2016**, *16*, 189.
[13] O. Zavorotynska, A. El-Kharbachi, S. Deledda, B. C. Hauback, *Int. J. Hydrogen Energy* **2016**, *41*, 14387.
[14] H.-W. Li, T. Matsunaga, Y. Yan, H. Maekawa, M. Ishikiriyama, S.-i. Orimo, *J. Alloys Compd.* **2010**, *505*, 654.
[15] I. Saldan, *Int. J. Hydrogen Energy* **2016**, *41*, 11201.
[16] X. Wang, X. Xiao, J. Zheng, X. Huang, M. Chen, L. Chen, *Int. J. Hydrogen Energy* **2020**, *45*, 2044.
[17] S.-J. Hwang, R. C. Bowman, J. W. Reiter, Rijssenbeek, G. L. Soloveichik, J.-C. Zhao, H. Kabbour, C. C. Ahn, *J. Phys. Chem. C* **2008**, *112*, 3164.
[18] M. Chong, A. Karkamkar, T. Autrey, S.-i. Orimo, S. Jalisatgi, C. M. Jensen, *Chem. Commun.* **2011**, *47*, 1330.
[19] G. Severa, E. Ronnebro, C. M. Jensen, *Chem. Commun.* **2010**, *46*, 421.
[20] J. Zheng, H. Cheng, X. Xiao, M. Chen, L. Chen, *Int. J. Hydrogen Energy* **2019**, *44*, 24292.
[21] F. Maximilian, Z.-K. Zhirong, R. Jianjiang, W. Arne, W. Peter, *Nanotechnology* **2009**, *20*, 204029.
[22] M. A. Wahab, Y. Jia, D. Yang, H. Zhao, X. Yao, *J. Mater. Chem. A* **2013**, *1*, 3471.
[23] Y. Yan, Y. S. Au, D. Rentsch, A. Remhof, P. E. de Jongh, A. Zuttel, *J. Mater. Chem. A* **2013**, *1*, 11177.
[24] S. Jeong, T. W. Heo, J. Oktawiec, R. Shi, S. Kang, J. L. White, A. Schneemann, E. W. Zaia, L. F. Wan, K. G. Ray, Y.-S. Liu, V. Stavila, J. Guo, J. R. Long, B. C. Wood, J. J. Urban, *ACS Nano* **2020**, *14*, 1745.
[25] J. Zheng, X. Xiao, L. Zhang, S. Li, H. Ge, L. Chen, *J. Mater. Chem. A* **2017**, *5*, 9723.
[26] M. Han, Q. Zhao, Z. Zhu, Y. Hu, Z. Tao, J. Chen, *Nanoscale* **2015**, *7*, 18305.

[27] K. G. Ray, L. E. Klebanoff, J. R. I. Lee, V. Stavila, T. W. Heo, P. Shea, A. A. Baker, S. Kang, M. Bagge-Hansen, Y. -S. Liu, J. L. White, B. C. Wood, *Phys. Chem. Chem. Phys.* **2017**, *19*, 22646.

[28] C. Sugai, S. Kim, G. Severa, J. L. White, N. Leick, M. B. Martinez, T. Gennett, V. Stavila, C. Jensen, *ChemPhysChem* **2019**, *20*, 1301.

[29] J. Yang, H. Fu, P. Song, J. Zheng, X. Li, *Int. J. Hydrogen Energy* **2012**, *37*, 6776.

[30] H. Y. Zhang, G. L. Xia, J. Zhang, D. L. Sun, Z. P. Guo, X. B. Yu, *Adv. Energy Mater.* **2018**, *8*, 1702975.

[31] Q. Zhang, Y. Huang, L. Xu, L. Zang, H. Guo, L. Jiao, H. Yuan, Y. Wang, *ACS Appl. Nano Mater.* **2019**, *2*, 3828.